Chapter I

Introduction

Introduction

Equilibrium has become an important concept in our models of chemistry and physics, allowing us to describe stable, stationary states of a physical system. Of importance to dynamic processes is how the system responds to a perturbation, or an input of energy, that pushes the system from its local equilibrium. For a molecule, this could be an absorption of a photon that places the molecule into an excited energetic state. If the molecule is perfectly isolated from its environment, the input energy remains within the molecule unless reemitted in the form of a photon. Due to coupling of the molecule with the environment, however, these excited states of the system are generally not persistent and will decay with time back toward either the ground state equilibrium or potentially toward a new equilibrium, which could take the form of a chemical change (e.g., isomerization, reactivity, etc.). This process by which energy is exchanged from the system under question to its environment is generally referred to as relaxation.[1–5] Understanding relaxation processes is key if we want to be able to control how energy input into a system can be transduced to do work. For molecular and materials systems, this could take the form of photoexcitation toward the generation of electron hole pairs that could be harvested for solar energy. Alternatively, the magnetic states of a molecular/material system can be manipulated with external fields for information storage and computing purposes.

This thesis explores disparate subjects, but all fall under the theme of understanding dissipative dynamics for a given application. Key tools are used to study these dynamic processes. As a result, we have dedicated this first chapter to descriptions of techniques that are endemic throughout this work: transient absorption (TA) spectroscopy and electron paramagnetic resonance (EPR) spectroscopy. We employed ultrafast TA measurements to study the evolution and relaxation of excited states in Chapters II, IV, and VI, looking at singlet fission in bipentacene

coordination complexes, Cu (I) bis-1,10-phenanthroline photosensitizers, and Ni (II) 2,2'-bipyridine complexes relevant to cross-coupling photocatalysis, respectively. In Chapter III, we employed continuous wave (CW) EPR and pulsed EPR to study magnetic relaxation in S = ½ qubit candidates copper (II) phthalocyanine and vanadyl phthalocyanine. In Chapter V, we explore the use of time-resolved EPR techniques to study high-spin triplet pair states that are generated via singlet fission.

Our discussion on TA spectroscopy centers around the general features observed in TA data and in the experimental setup required to perform data collection. For a rigorous theoretical treatment of TA, the reader is referred to other resources. For EPR, we delve into the origins of the spin Hamiltonian before discussing EPR spectroscopy and magnetic relaxation processes. We use the spin Hamiltonian formulation to fit data and frame our discussion on S = ½ systems in Chapter III. Additionally, we leverage the background presented here to explicitly derive the spin operators and Hamiltonian for triplet pair states, presented in Appendix C as companion to the singlet fission TREPR data of Chapter V.

Transient Absorption

Transient absorption (TA) spectroscopy is a technique used to probe the time-dependent absorption profile of a sample after it is excited by a pulsed laser.[6] The transient species generated by the excitation pulse can persist across a wide range of timescales, and we will focus on two: the ultrafast sub-picosecond regime and the nanosecond to millisecond regime. We will focus mostly on the general features of femtosecond transient absorption (fsTA) spectroscopy before detailing the spectrometer setup for fsTA and nanosecond transient absorption (nsTA) used in our lab. In common practice for fsTA, a narrow bandwidth pulsed laser source is used to provide the initial

excitation energy to the sample (the pump pulse), and a broadband white light pulse is used as the probe (Figure 1.1).

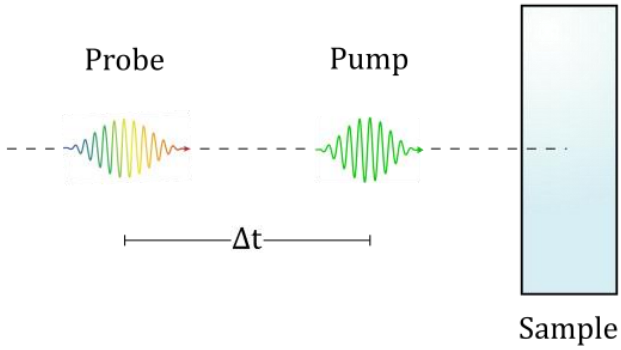

Figure 1.1 The narrow bandwidth pump and broad bandwidth probe pulses used in TA spectroscopy are spatially overlapped at the sample and then varied in temporal overlap (Δt) to generate the TA spectrum.

The pump and probe light are spatially overlapped at the sample such that the volume of sample that is excited by the pump pulse is also sampled by the probe. The timing delay (Δt) between the pump and probe may then be systematically varied to monitor the evolution of the absorption profile over time caused by the pump. Just as in steady-state absorption spectroscopy, the intensity of the various frequencies of light distributed in the probe will change by interacting with the sample. In this case, though, we have generated a nonequilibrium population in which a fraction of the molecules or species in our sample have been excited by the pump. As a result, the probe will be modulated by the presence of both ground and excited state species (Figure 1.2A).[6]

As we are interested in following the evolution of the excited states in the sample, the TA data is collected as a difference spectrum by subtracting the transmittance of light detected in a

shot with the pump on the sample ($T_{pump\ on}$) minus the intensity of light detected in a shot with the pump blocked from the sample ($T_{pump\ off}$), the latter of which should reflect the ground state absorption spectrum. This is written out in the equations below. The TA spectrum may be presented in terms of the change in transmittance (ΔT) or the change in absorbance (ΔA). All data presented in the following work is presented as ΔA or equivalently the change in optical density (ΔOD).

$$T = \frac{I}{I_0}$$

$$A = -\log(T) = \log\left(\frac{I_0}{I}\right)$$

$$\Delta T = T_{pump\ on} - T_{pump\ off} = \left(\frac{I}{I_0}\right)_{pump\ on} - \left(\frac{I}{I_0}\right)_{pump\ off}$$

$$\Delta A = A_{pump\ on} - A_{pump\ off} = \log\left[\left(\frac{I_0}{I}\right)_{pump\ on}\right] - \log\left[\left(\frac{I_0}{I}\right)_{pump\ off}\right]$$

$$\Delta A = \log\left[\left(\frac{I_0}{I}\right)_{pump\ on} \cdot \left(\frac{I}{I_0}\right)_{pump\ off}\right]$$

$$\Delta A = -\log\left(\frac{I_{pump\ on}}{I_{pump\ off}} \cdot \frac{I_{0_{pump\ off}}}{I_{0_{pump\ on}}}\right) \qquad Eqs.\ 1.1A - F$$

First, we define the standard expression for transmittance (T) and absorbance (A) in terms of the intensity of light after passing through the sample (I) and the intensity of light incident on the sample (I_0). Next, we define ΔT and ΔA in terms of the intensity of light passing through the sample with the pump on ($I_{pump\ on}$), the intensity of light passing through the sample with the pump off ($I_{pump\ off}$), the intensity of light incident on the sample with the pump on ($I_{0_{pump\ on}}$),

and the intensity of light incident on the sample with the pump off ($I_{0_{pump\ off}}$). As written in the expression for ΔA, the ratios $\frac{I_{pump\ on}}{I_{pump\ off}}$ and $\frac{I_{0_{pump\ off}}}{I_{0_{pump\ on}}}$ can be experimentally determined at a detection channel after the sample and at a reference detection channel, respectively.

The signal that arises in TA spectroscopy comes from the third-order nonlinear susceptibility in the light-matter interaction.[7] We will focus here on the general features observed in a transient absorption spectrum, which are ground state bleach (GSB), stimulated emission (SE), and excited state absorption (ESA), which is sometimes equivalently referred to as photoinduced absorption (PIA) (Figure 1.2). A GSB feature appears as a negative ΔA signal, generally aligns with the steady-state absorption profile of the sample and arises due to loss of ground state absorbing species due to the excitation. At a given wavelength in the bleach, there will be a greater number of photons passing through the sample with the pump on due to the reduction in population of ground state species than with the pump off ($I_{pump\ on} > I_{pump\ off}$), which leads to a negative ΔA signal as shown in the above expression. SE arises if the excited state species has an electric dipole-allowed transition back to the ground state. If this is the case, the radiation field in the probe can induce a transition from the excited state to the ground state along with the emission of a photon. As with the bleach, at a given wavelength in the SE feature, $I_{pump\ on} > I_{pump\ off}$ and SE will appear as a negative ΔA signal. ESA occurs when the radiation field of the probe pulse interacts with an excited state species generated by the pump and induces a dipole allowed transition from the excited state to an energetically higher lying excited state along with absorption of a photon. In this case, in the wavelength range covered by the ESA, $I_{pump\ on} < I_{pump\ off}$ and the ESA will appear as a positive ΔA signal (Figure 1.2B). The features in TA may have substantial overlap with each other.

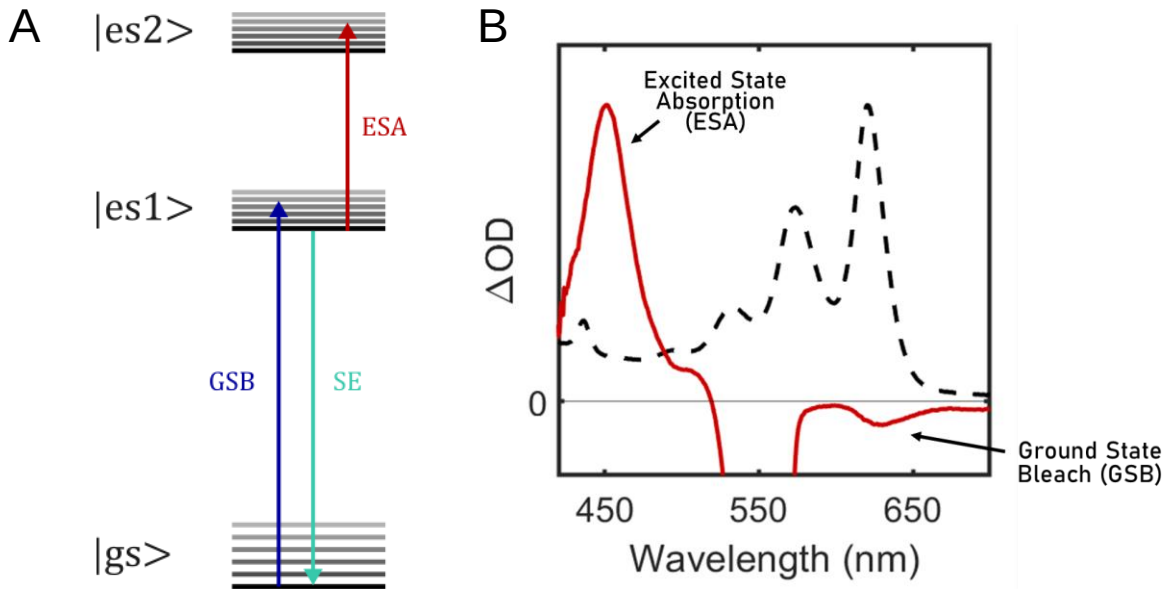

Figure 1.2 (A) A generalized Jablonski diagram depicting the various processes that can occur in TA spectroscopy. Here, we denote the ground state as |gs>, first excited state as |es1>, and the higher lying excited state as |es2>. **(B)** An example of the comparison between the ground state absorption spectrum (dashed black lines) and a time cut of the visible TA spectrum (solid red lines) of a pentacene derivative with a highlight given to the GSB and ESA features in the TA spectrum. The large negative feature centered around 550 nm is residual pump scatter.

Observing the change in intensity and spectral shape of the transient absorption features over time provides important kinetic information regarding the excited state relaxation processes at play in a given sample. For example, different excited states may exhibit distinct ESA features in the transient spectra, allowing us to ascertain which states may be populated following excitation and correlate their interconversion. The absolute assignment of an ESA feature is challenging, however, and requires supplementary experimental and/or computational validation.

Femtosecond Transient Absorption Setup

We will now discuss the experimental setup used throughout the work in this thesis to collect femtosecond transient absorption (fsTA) data in addition to some of the features of fsTA that are unique to probing ultrafast timescales. A general layout of the laser and fsTA spectrometer design is presented in Figure 1.3.

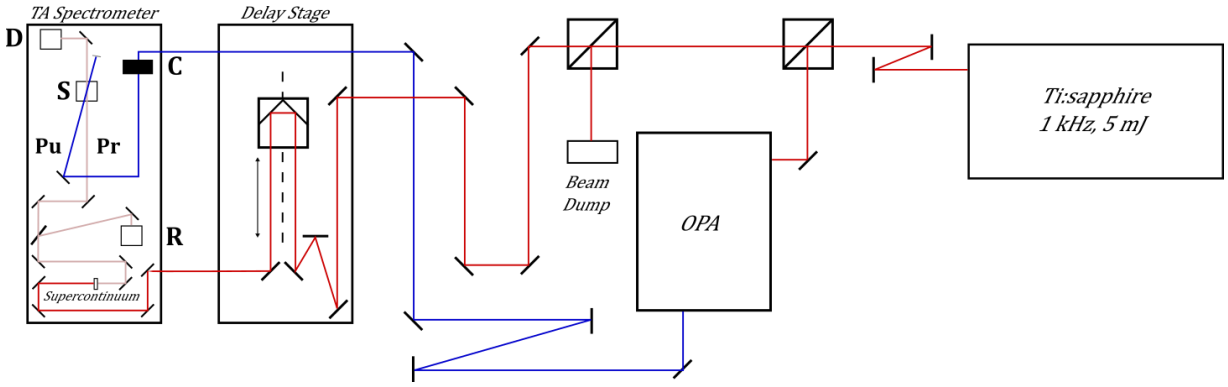

Figure 1.3 The general overview of the fsTA setup including Ti:sapphire laser source, OPA, delay stage, and TA spectrometer. Red lines represent 800 nm fundamental of the Ti:sapphire laser, blue represent variable wavelength output of the OPA used as the pump (**Pu**), and pink represent the supercontinuum probe (**Pr**). **D** ≡ detector channel, **S** ≡ sample, **C** ≡ chopper, **R** ≡ reference channel.

The source of both the pump and probe pulses utilized in the fsTA spectrometer is ultimately a femtosecond pulsed Ti:sapphire laser (Coherent Astrella, 5 mJ output, 1000 Hz repetition rate) with a maximum wavelength around 800 nm. The output of this Ti:sapphire laser is split by a 50:50 beamsplitter. Half of the beam is sent to an optical parametric amplifier (OPA, OPerA Solo), which is used to generate wavelength-tunable narrow bandwidth pump pulses, and the other half is used to generate the white light probe.

The OPA provides multiple options for the pump beam: either the signal or idler can be used directly or converted to higher frequencies via second harmonic generation (SHG), fourth harmonic generation (taking the SHG of the SHG), or sum frequency generation (SFG) by combining signal or idler with an additional portion of 800 nm light. With these options, the OPA can cover a wide range of output wavelengths from ~250 – 3000 nm.

The output of the OPA is routed into TA spectrometer (Helios Fire, Ultrafast Systems) where it is chopped using a mechanical chopper operating at 500 Hz, half of the repetition rate of the laser. The chopper functions to block every other shot of the pump so that the data can be divided into shots with pump on and shots with pump off. A neutral density filter allows for control over the final power incident at the sample.

The probe is generated using the other half of the 800 nm outputted from the Ti:sapphire laser. It is attenuated by another beamsplitter before being focused using telescoping lenses and routed into a physical delay stage. The delay stage consists of a set of mirrors mounted on a motorized track. Changing the position of the mirrors on the track changes the pathlength of the probe leg of the spectrometer and ultimately the timing between the arrival of the pump and probe pulses at the sample (Δt). The timing available is such that Δt's may be sampled in a positive (probe arrives at the sample after the pump) and negative (probe arrives at the sample before the pump) with time zero being the point at which pump and probe are directly overlapped in time at the sample. In a standard run, the time window (maximally out to 7.7 ns) can be selected and the delay stage is progressively moved along as a function of collection, building each time point successively. After the delay stage the 800 nm light is passed through an iris and neutral density filter onto a supercontinuum generating medium. The medium is different depending on the

wavelength range required of the probe spectrum (e.g., a CaF_2 plate is used for UV probe generation from 300 – 700 nm, a sapphire plate for visible probe generation from 400 – 800 nm).

There are three probes available: UV, visible, and NIR. Once the supercontinuum is generated it is passed through a filter to remove excess 800 nm light, and it is split into half that is focused through the sample and half that is focused into a reference channel. In both the sample and reference channels, a confocal mirror focuses the probe onto a fiber optic that leads to a diffraction grating and ultimately to a CCD array detector. The UV and visible probes utilize the same set of sample and reference detectors, and the NIR channel utilizes its own gratings and detectors.

Other Features in Femtosecond Transient Absorption Spectra

There are several other phenomena that impact fsTA datasets, some of which are unique to this ultrafast technique. The first we will discuss is group velocity dispersion (or temporal chirp), then cross-phase modulation, two-photon absorption, and stimulated Raman effects. Because we use a broadband probe, there are a wide range of wavelengths traveling in the white light pulse. In condensed media, the speed of light is not uniform but rather dependent on the wavelength of light. The result of this is that the blue end of the probe moves at a higher velocity than the red end. In other words, the shorter wavelength light will reach the sample and hit the detector at earlier times than the longer wavelengths in the probe. The chirp spreads the wavelengths of the probe on the time scales of hundreds of femtoseconds, and as a result, time zero in the spectrum will also be wavelength dependent. This effect is not distinguishable in spectroscopies with slower time resolution but contributes to the data matrix collected in fsTA.[8]

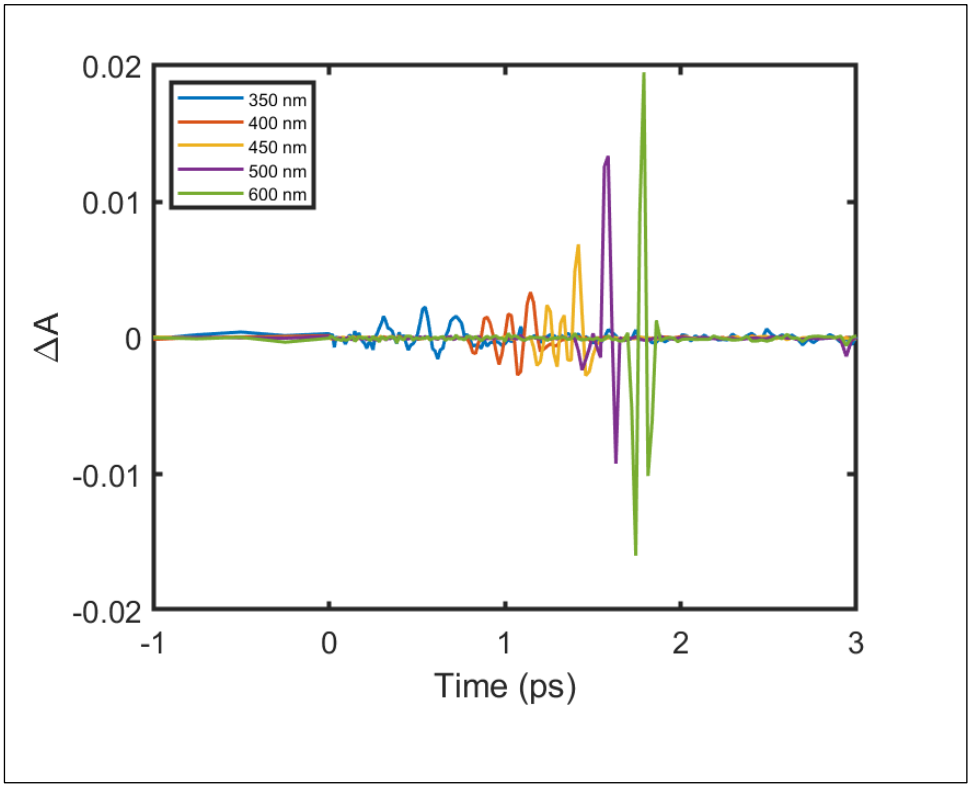

Figure 1.4 A plot of XPM observed in a THF sample with 550 nm pump along the time axis at 350, 400, 450, 500, and 600 nm. The temporal chirp can be observed as time zero is dependent on wavelength. The shape and width of the XPM signal is also dependent on the chirp.

Cross-phase modulation (XPM) is a nonlinear effect that occurs in fsTA because of the high photon densities available in the femtosecond pulses. XPM occurs in the probe pulse when it is spatially and temporally overlapped (at time zero) with the pump. The high electric field amplitude of the pump modulates the distribution of frequencies in the probe spectrum when they simultaneously interact at the sample. As a result, portions of the probe spectrum can have more or fewer photons when the pump is on the sample than when it is blocked, leading to an oscillatory pattern in the ΔA spectrum along both the time and wavelength axes (Figure 1.4). The XPM is

observable around delay time zero and allows us to follow the temporal chirp in a solvent blank sample.[8]

Other nonlinear effects can occur due to the spatial and temporal overlap of the pump and the probe including two photon absorption and stimulated Raman processes. Two photon absorption will appear as a positive ΔA signal, whereas stimulated Raman, like SE, will appear as a negative ΔA signal. The positions of these features are generally dependent on the pump wavelength being used. As with XPM, these features only persist around time zero and are generally modeled to decay within the instrument response time.[8]

Nanosecond Transient Absorption Setup

In addition to the Helios Fire fsTA spectrometer, we also can perform nsTA (EOS, Ultrafast Systems). The same pump pulse generated by the OPA is used as in the fsTA spectrometer. The probe, however, is generated using a white light laser that is focused onto the sample. The timing between pump and probe is then controlled digitally, allowing the buildup of the two-way dataset. The timing delay is not continuously swept through the time window of the experiment (maximally out to 500 μs) as the delay stage is in fsTA. Rather, the time delay sporadically fills in time points in the window and the dataset is progressively averaged.

Some Remarks on Data Analysis

In our TA setup, the signal is collected via diffraction of the white light probe onto a CCD array detector, allowing for easy construction of a two-dimensional data matrix along wavelength and time axes. If features in the TA spectrum are well resolved from each other, single wavelength exponential fitting may provide access to the relevant rate constants describing the evolution of the data. Often, there may be substantial overlap between spectral features in the data. Time

components of various decay processes may also be close and difficult to distinguish in a wavelength cut of the data. In this case, global and target kinetic analyses offer a powerful tool for fitting the TA data matrix to a prescribed physicochemical model. In both global and target kinetic analyses, the entire data matrix is fit along all times and wavelengths simultaneously, allowing us to fit spectral and time components based off of correlated changes in the data.[9–11]

There are some fundamental assumptions regarding the nature of TA data that we should review before discussing how kinetic analysis is applied to a given system. Much like steady-state absorption, we presume that the difference absorption spectra observed by TA are still described by the Beer-Lambert law that relates the absorbance (or differential absorbance ΔA) to the extinction coefficient at a given wavelength $\varepsilon(\lambda)$, the pathlength of the sample l, and the concentration of the absorbing species c. In TA spectroscopy, we examine the time-dependent evolution of the various photoexcited species by tracking their absorption difference spectra as a function of time. As such, the concentration c of the observed species will change over time given available relaxation pathways, and this parameter is best described by a time-dependent function, $c(t)$.

$$\Delta A(\lambda, t) = \varepsilon(\lambda) * l * c(t) \qquad Eq. 1.2$$

When there is more than one excited state being probed, the Beer-Lambert law describing the differential absorbance across the spectrum is summed over the number of species i.

$$\frac{\Delta A(\lambda, t)}{l} = \sum_i \varepsilon_i(\lambda) * c_i(t) \qquad Eq. 1.3$$

Here, we have omitted the optical pathlength l – as the excited state species are all generated in the same sample holder, this value is the same over all i components being summed

and can simply be treated as a scaling term absorbed into ΔA. An assumption implicit in this model is that ΔA is bilinear in functions of wavelength and time. That is to say that $\varepsilon_i(\lambda)$ are functions solely dependent on λ and that $c_i(t)$ are solely dependent on t so that these two sets of functions are independent of each other. This presumed separability belies much of the analytical techniques for decomposing the transient absorption data matrix. This separability inherently breaks down in ultrafast TA, but can be corrected or parameterized in a given model.

As discussed, the speed of light in condensed media is dependent on the wavelength of light, a phenomenon known as group velocity dispersion or temporal chirp. This chirp spreads the wavelengths on the time scale of hundreds of femtoseconds and would not be distinguishable with slower time resolution spectroscopies. As a result of the dispersion, the spectral shapes in the data become dependent on time and not just wavelength, i.e. $\varepsilon_i(\lambda) \rightarrow \varepsilon_i(\lambda, t)$. Commonly, the dispersion curve is fitted to a polynomial and the time axis is corrected for each wavelength accordingly. This reinstates the separability of the wavelength- and time-dependent functions in the above equation, aiding the decomposition of the data into linearly independent components. Otherwise, the dispersion curve needs to be parametrized and accounted for in the fitted model for data analysis.

Global and target kinetic analyses are a critical part of the toolkit for fitting transient absorption datasets. Both global and target analyses use nonlinear least squares fitting to find the best fit set of parameters to describe the dataset according to a particular kinetic model. Most often in the case of photophysical processes, we assume first order kinetics, which leads to exponential decay behavior. In the case of global kinetic analysis, the model applied is a sum of i exponentially decaying components. This is equivalent to a kinetic model in which there are i species that are decaying in parallel with each other, i.e. there is no conversion between the excited state species,

there is only decay back to the ground state. The expression for ΔA is given below and the fitted spectral components are referred to as decay associated spectra (DAS) or sometimes in the case of difference data decay associated difference spectra (DADS).[9]

$$\Delta A = \sum_i DAS_i \cdot e^{-k_i t} \qquad Eq.1.4$$

Although the parallel model may be physically relevant for some systems, it does not always map one-to-one with the physically relevant model for a given system. Target kinetic analysis implies the application of such a model. The simplest model to apply is a sequential one, in which the initially photoexcited species decays into the next excited state species and so on in tandem until the last species finally decays back to the ground state. Here the spectrally fit components are generally referred to as evolution associated spectra (EAS) or evolution associated difference spectra (EADS). The fitted kinetic components are identical between the parallel and sequential model. The major difference is that the EAS will be formed from linear combinations of the DAS. Once the kinetic model has converged to describe the trajectory of excited state species that are formed in the photodynamics, the spectra may be referred to as species associated spectra (SAS) or species associated difference spectra (SADS).[9]

In summary, in this section we have reviewed the general features of TA data, the experimental setup for TA data collection, and some general concerns regarding the analysis of TA data.

Spin Hamiltonian

The study of systems containing unpaired spins is greatly aided by the formalism of a spin Hamiltonian. The spin Hamiltonian expresses the interactions within the subsystem of unpaired

electrons solely in terms of electron spin operators. This formalism is commonly encountered in magnetic resonance spectroscopies as a tool to fit experimental data, as it allows for the description of the small energetic differences that arise due to spin-dependent interactions without calculation of the full molecular Hamiltonian.[12]

Electron Spin Angular Momentum

One of the simplest cases to begin our discussion of spin angular momentum is that of a single electron. The spin angular momentum for this lone electron can be visualized as a vector in three-dimensional Cartesian coordinates and is characterized by its magnitude and orientation defined by the x-, y-, and z-components of the vector. In quantum mechanics, the magnitudes of these components are quantized when acted upon by their respective operators. For example, the operator $\hat{S}_z$ acting on a given wavefunction returns the magnitude of the z-component of the spin angular momentum. The same goes for $\hat{S}_x$ and $\hat{S}_y$ that describe the x- and y-components of the spin, respectively. The spin angular momentum operator $\hat{S}$ can then be written as a vector containing the $\hat{S}_x$, $\hat{S}_y$, and $\hat{S}_z$ operators much as one would use a three-dimensional column vector to describe the x-, y-, and z-coordinates for a Cartesian vector.[12–16] However, we can only observe one of the three components (Figure 1.5), as follows.

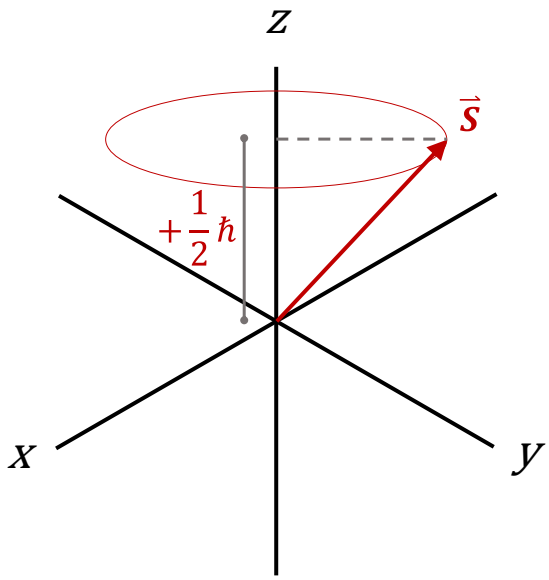

Figure 1.5 The total spin angular momentum, $\vec{S}$, of an electron represented as vector along the 3D Cartesian axes. The z-component of the spin angular momentum is labeled as $+\frac{1}{2}\hbar$. As we have drawn it here, this vector represents the spin in the $|\alpha\rangle$ or $\left|+\frac{1}{2}\right\rangle$ state. By defining the z-component of the spin angular momentum, the x- and y-components are undefined. As a result, the spin vector lies anywhere along the red circle (see text).

The spin operators for a single electron are given by the Pauli matrices and by convention are given in a basis that diagonalizes $\hat{S}_z$. Two eigenstates are returned when operated on by $\hat{S}_z$, either $+\frac{1}{2}\hbar$ or $-\frac{1}{2}\hbar$, and these states can be denoted as $|\alpha\rangle$ and $|\beta\rangle$, respectively (in the literature they may also be labeled by the m_s eigenvalue $\left|+\frac{1}{2}\right\rangle$, $\left|-\frac{1}{2}\right\rangle$). Here, and for the remainder of this thesis, we will write these operators and any resulting Hamiltonians in units of $\hbar$.[14]

$$\hat{S}_x = \frac{1}{2}\begin{bmatrix} 0 & 1 \\ 1 & 0 \end{bmatrix}$$

$$\hat{S}_y = \frac{i}{2}\begin{bmatrix} 0 & -1 \\ 1 & 0 \end{bmatrix}$$

$$\hat{S}_z = \frac{1}{2}\begin{bmatrix}1 & 0\\ 0 & -1\end{bmatrix} \qquad Eqs.\,1.5A - C$$

The square of the total spin (the square root of which gives the magnitude of the overall spin vector) is described by the operator $\hat{S}^2$ and is equal to the scalar product of the spin vector with its transpose. This gives the sum of the squares of the x-, y-, and z-components of the spin and is analogous to the Pythagorean theorem in three dimensions.

$$\hat{S}^2 = \hat{S}\cdot\hat{S} = \begin{bmatrix}\hat{S}_x & \hat{S}_y & \hat{S}_z\end{bmatrix}\begin{bmatrix}\hat{S}_x\\ \hat{S}_y\\ \hat{S}_z\end{bmatrix} = \hat{S}_x^2 + \hat{S}_y^2 + \hat{S}_z^2 \qquad Eq.\,1.6A$$

The $\hat{S}^2$ operator for the one electron case is written explicitly below.

$$\hat{S}^2 = \frac{3}{4}\begin{bmatrix}1 & 0\\ 0 & 1\end{bmatrix} \qquad Eq.\,1.6B$$

For a general spin system, the eigenvalue of the $\hat{S}^2$ operator is $S(S+1)$ when acting on a given spin state where S is the total spin quantum number of the state. The $\hat{S}_z$ operator reports on the total spin projection number M_s of a given eigenstate, and its eigenvalues will span $M_s \in \{-S,\ -(S-1),\ \dots,\ S-1,\ S\}$.

The commutation relations for the spin operators are as follows:

$$\left[\hat{S}^2, \hat{S}_x\right] = \left[\hat{S}^2, \hat{S}_y\right] = \left[\hat{S}^2, \hat{S}_z\right] = 0$$

$$\left[\hat{S}_x, \hat{S}_y\right] = \hat{S}_x\hat{S}_y - \hat{S}_y\hat{S}_x = i\hbar\hat{S}_z$$

$$\left[\hat{S}_y, \hat{S}_z\right] = \hat{S}_y\hat{S}_z - \hat{S}_z\hat{S}_y = i\hbar\hat{S}_x$$

$$\left[\hat{S}_z, \hat{S}_x\right] = \hat{S}_z\hat{S}_x - \hat{S}_x\hat{S}_z = i\hbar\hat{S}_y \qquad Eqs.\,1.7A - D$$

A representative calculation of $[\hat{S}_x, \hat{S}_y]$ is provided below. As shown, the order of operations matters. Application of the $\hat{S}_x$ operator followed by $\hat{S}_y$ does not lead to the same result as $\hat{S}_y$ followed by $\hat{S}_x$.

$$\hat{S}_x\hat{S}_y - \hat{S}_y\hat{S}_x = \frac{1}{2}\hbar\frac{1}{2}\hbar\begin{bmatrix}0 & 1\\ 1 & 0\end{bmatrix}\begin{bmatrix}0 & -i\\ i & 0\end{bmatrix} - \frac{1}{2}\hbar\frac{1}{2}\hbar\begin{bmatrix}0 & -i\\ i & 0\end{bmatrix}\begin{bmatrix}0 & 1\\ 1 & 0\end{bmatrix}$$

$$\hat{S}_x\hat{S}_y - \hat{S}_y\hat{S}_x = \frac{1}{4}\hbar^2\begin{bmatrix}i & 0\\ 0 & -i\end{bmatrix} - \frac{1}{4}\hbar^2\begin{bmatrix}-i & 0\\ 0 & i\end{bmatrix}$$

$$\hat{S}_x\hat{S}_y - \hat{S}_y\hat{S}_x = \frac{1}{4}\hbar^2\begin{bmatrix}2i & 0\\ 0 & -2i\end{bmatrix} = \frac{1}{2}i\hbar^2\begin{bmatrix}1 & 0\\ 0 & -1\end{bmatrix} = i\hbar\hat{S}_z \qquad Eq.\,1.8$$

Simultaneous measurement can only be made with operators that commute with each other, and thus have simultaneous eigenfunctions. Operators that commute relate to observable quantities that are statistically independent of each other, and thus the measurement of one does not impact the outcome of the measurement of the other, (i.e. the order of operations does not matter). These commutation relations demonstrate that the square of the total spin operator $\hat{S}^2$ can commute with any of the spin operators $\hat{S}_x$, $\hat{S}_y$, and $\hat{S}_z$; however, the operators $\hat{S}_x$, $\hat{S}_y$, and $\hat{S}_z$ do not commute with each other and as a result, the projection of the spin angular momentum onto all three Cartesian axes cannot be known simultaneously. This means that if the *z*-component of the spin angular momentum is measured, the spin projections onto the *x* and *y* axes are completely indeterminant (Figure 1.5). The *z*-axis is conventionally taken as the axis of quantization, and so the eigenvalues of the $\hat{S}^2$and $\hat{S}_z$ operators are used to define unique spin states in the spin Hamiltonian formalism.

For multispin systems, the total spin S is taken to be the sum of the individual electron spins:

$$Eq.\,1.9A$$

$$S = S_1 + S_2 + \cdots + S_n$$

This applies as well to the Cartesian components of the spin vector. For calculating the matrices for higher spin systems, this sum is to be taken as the Kronecker sum of the individual spin matrices (e.g., $S = S_1 \otimes I + I \otimes S_2$).

$$S_{x,y,z} = S_{1x,y,z} + S_{2x,y,z} + \cdots + S_n \qquad Eq.\,1.9B$$

From these equations, we can build spin operators for spin systems of higher multiplicity, which we can further apply in the construction of effective spin Hamiltonians.[14]

Electron-Magnetic Field Interaction: The Zeeman Hamiltonian

The intrinsic electron spin angular momentum gives rise to a magnetic dipole moment. Because of the negative charge of the electron, the electron magnetic dipole moment μ is aligned antiparallel to the total spin angular momentum $\vec{S}$. The explicit relationship between the spin angular momentum and the magnetic moment is given below where g_e is the electron g-factor (nearly 2.0023) and μ_B the Bohr magneton (9.27 x 10^{-27} m^2 A).

$$\vec{\boldsymbol{\mu}} = -g_e \mu_B \vec{\boldsymbol{S}} \qquad Eq.\,1.10$$

The magnetic moment gives intuition for how the system will behave in the presence of an externally applied magnetic field $\boldsymbol{B_0}$. Upon application of the external field, the magnetic moment will align with the field, by convention the z-axis. The two eigenstates of the system ($\left|+\frac{1}{2}\right\rangle$, $\left|-\frac{1}{2}\right\rangle$) will then be split in energy; this is known as the electronic Zeeman splitting. The $\left|-\frac{1}{2}\right\rangle$ state will have the z-component of its magnetic moment aligned parallel to $\boldsymbol{B_0}$, whereas the $\left|+\frac{1}{2}\right\rangle$ will have the z-component of its magnetic moment aligned antiparallel to $\boldsymbol{B_0}$ (Figure 1.6).

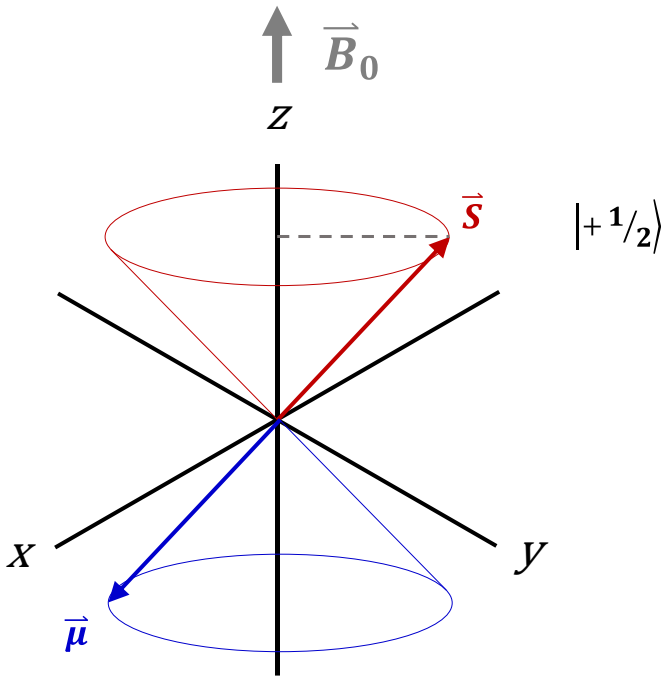

Figure 1.6 The electron magnetic dipole moment can be represented as a vector aligned antiparallel to the electron total spin angular momentum $\vec{S}$, shown here for the $|\alpha\rangle$ or $\left|+\frac{1}{2}\right\rangle$ state. The antiparallel alignment of the magnetic moment with the field raises the energy of this state relative to the parallel alignment in $|\beta\rangle$ or $\left|-\frac{1}{2}\right\rangle$.

The classical potential energy of a magnetic dipole in an external magnetic field is given by the following relationship.

$$U = -\vec{\mu} \cdot \vec{B} = g_e \mu_B \vec{S} \cdot \vec{B}_0 \qquad Eq. 1.11$$

In quantum mechanics, operators represent physical observables. The Hamiltonian operator for the Zeeman interaction, $\hat{H}_{zee}$, can therefore be written in terms of the spin angular momentum operators defined above, replacing the vector arrow notation with bolded symbols and

assuming an isotropic Zeeman interaction (i.e., invariant with respect to rotation as is the case for a free electron).

$$\hat{H}_{zee} = g_e \mu_B \boldsymbol{B^T} \cdot \boldsymbol{S}$$

$$\boldsymbol{S} = \begin{bmatrix} \hat{S}_x \\ \hat{S}_y \\ \hat{S}_z \end{bmatrix}$$

$$\boldsymbol{B} = \begin{bmatrix} B_x \\ B_y \\ B_z \end{bmatrix}$$

In addition to the spin angular momentum, the magnetic moment in a molecule includes orbital angular momentum due to the motion of charged electrons around the nucleus represented by the operators $\hat{L}^2, \hat{L}_x, \hat{L}_y, \hat{L}_z$. These operators have the same rules and commutators as spin angular momentum operators; in fact, these definitions exist for any quantum mechanical description of angular momentum. The magnetic moment arising from orbital motion couples to the electron spin magnetic moment (spin-orbit coupling). When orbital angular momentum is significant, the spin and orbital degrees of freedom may be summed by the standard rules of angular momentum addition to give the total angular momentum of the system $J = L + S$. This is often necessary in the case of free metal and lanthanide ions. Non-zero angular momentum arises from degeneracy in the ground state. For transition metal ions in a coordination complexes, the ligand field lifts the degeneracy present in the free ion, "quenching" the orbital angular momentum. Still, coupling between the ground electronic state and higher lying electronic states can yield small orbital angular momentum contributions that can be treated perturbationally.[12]

We can conceptualize the interaction of the electron spin with the orbital-induced magnetic fields as a perturbation of the effective magnetic field ($\boldsymbol{B_{eff}}$, differing from $\boldsymbol{B_0}$) experienced at the electron. Because the orbital degrees of freedom are spatially parametrized in the molecular frame, the $\boldsymbol{B_{eff}}$ experienced by the electron may be different in the molecular x-, y-, and z-directions given the orbital polarization. This means that the Zeeman response of the electron spin will be anisotropic and dependent on the orientation of the molecule with respect to the external field. As suggested, this dependence could be parametrized in a $\boldsymbol{B_{eff}}$ in the spin Hamiltonian, although it is equivalent to put the orientation dependence on the g value. In this case, the free electron g-value g_e is replaced by a 3×3 Cartesian $\boldsymbol{g}$ tensor as below:[14]

$$\widehat{H}_{zee} = \mu_B \boldsymbol{B^T} \cdot \boldsymbol{g} \cdot \boldsymbol{S}$$

$$\boldsymbol{g} = \begin{bmatrix} g_{xx} & g_{xy} & g_{xz} \\ g_{yx} & g_{yy} & g_{yz} \\ g_{zx} & g_{zy} & g_{zz} \end{bmatrix} \qquad Eq.\,1.13$$

The theoretically defined $\boldsymbol{g}$ tensor may have antisymmetric components. However, single crystal EPR measurements that probe orientation-dependent transitions measure the energetic separation of the Zeeman split sublevels and indirectly provide information on the matrix product $\boldsymbol{g} \cdot \boldsymbol{g^T}$, which is always symmetric. The experimental $\boldsymbol{g}$ tensor is derived from the experimentally-determined $\boldsymbol{g} \cdot \boldsymbol{g^T}$, and as a result, the experimentally-derived $\boldsymbol{g}$ tensor is always symmetric as well (i.e. $g_{xy} = g_{yx}, g_{xz} = g_{zx}, g_{yz} = g_{zy}$) and still reproduces the experimental spectrum. As for any real, symmetric matrix, $\boldsymbol{g} \cdot \boldsymbol{g^T}$ and $\boldsymbol{g}$ are diagonalizable and can be given in their principal frame:

$$\boldsymbol{g} = \begin{bmatrix} g_x & 0 & 0 \\ 0 & g_y & 0 \\ 0 & 0 & g_z \end{bmatrix} \qquad Eq.\,1.14A$$

Thus, the tensor can be fully parameterized by three values (g_x, g_y, g_z), and the full $\boldsymbol{g}$ tensor can be produced by any arbitrary rotation (R) of the principal axis system to the direction of the applied field.

$$\boldsymbol{g^{rot}} = R\boldsymbol{g}R^T \qquad Eq.\,1.14B$$

The classification of EPR spectra is typically done with respect to the symmetry of the g tensor. As previously mentioned, in the case where all principal values of $\boldsymbol{g}$ are equal ($g_x = g_y = g_z$), the system is termed isotropic. When two of the principal values are equivalent, the unique axis is taken as the z-axis ($g_x = g_y \neq g_z$) and the system is termed axial. For axial systems, it is common to refer to the principal g values rather as parallel or perpendicular ($g_{\parallel} = g_z, g_{\perp} = g_x = g_y$). Finally, when all three of the principal g values are distinct ($g_x \neq g_y \neq g_z$), the system is termed rhombic.[14]

Perturbative treatment of the spin-orbit coupling (SOC) provides a means of assessing which orbital wavefunctions are admixed into the ground state by the magnetic field (this depends on the nature of the orbital and the corresponding orbital angular momentum operators $\hat{L}_x, \hat{L}_y, \hat{L}_z$). As such, this procedure also gives a general expression for the elements of $\boldsymbol{g}$:[17]

$$g_i = g_e - \lambda \sum_{e \neq g} \frac{\langle \psi_g | \hat{L}_i | \psi_e \rangle \langle \psi_e | \hat{L}_i | \psi_g \rangle}{E_g - E_e} \qquad Eq.\,1.15A$$

Here, λ is the many-electron SOC constant ($\lambda = \pm\frac{\zeta}{2S}$ where ζ is the one-electron SOC constant for a given atom), ψ_g and ψ_e represent the ground state and excited state orbital wavefunctions, respectively; $\hat{L}_i$ is the orbital angular momentum operator for $i = x, y, z$; and E_g and E_e represent the energies of the ground and excited state orbitals, respectively. For a transition

metal complex, the orbital wavefunctions being summed over are generally the *d* orbitals. These sums have been calculated and give predictable integer values for a given combination of ground and excited orbital configurations. As such, this expression is sometimes represented in a simplified form as below:

$$g_i = g_e - \frac{n\lambda}{\Delta E} \qquad Eq.\,1.15B$$

Here, n is an integer coefficient that comes from the perturbation treatment and depends on which orbitals are mixed, and ΔE is the energetic separation between the states that are mixed. Additional terms may be added to the numerator of the fraction in this expression to account for covalency, *i.e.*, delocalization of the unpaired electron onto ligand-based orbitals.

Electron-Nucleus Interactions: Hyperfine Hamiltonian

Additional terms arise in the spin Hamiltonian due to an array of magnetic interactions that are possible within a molecule. The magnetic moments arising from nuclear spins within a paramagnetic molecule can interact with those of the electron spin system. This is known as the hyperfine interaction. As we did for the Zeeman interaction, we can define a hyperfine Hamiltonian $\widehat{H}_{HF}$ in terms of the electron spin operators ($\boldsymbol{S}$) and the nuclear spin operators ($\boldsymbol{I}$). The nuclear spin operators are defined just as the electron spin operators with I and M_I defining the total nuclear spin and magnetic sublevel, respectively.

$$\widehat{H}_{HF} = \boldsymbol{S} \cdot \boldsymbol{A} \cdot \boldsymbol{I} \qquad Eq.\,1.16$$

Just as we defined the g-tensor to describe the directional relationship between external field and electron spin, we define a hyperfine tensor $\boldsymbol{A}$ to describe the interaction between electron and nuclear spin. As with the g-tensor, the A tensor can be defined in its principal frame, which is

commonly taken to be aligned with the principal frame of the g tensor, although this is not strictly the case in low symmetry. Similarly, the principal values that define the A tensor can be isotropic, axial, or rhombic depending on the symmetry of the system. The isotropic components of the A tensor derive from a "contact term" defined by Fermi that requires the unpaired electron have non-zero probability density at the nucleus, which can only occur for *s*-orbitals or molecular orbitals with *s*-atomic orbital character admixed into the wavefunction. The anisotropic components of the A tensor arise from dipolar interactions between the electron and nuclear dipole. The general experimental impact of the hyperfine Hamiltonian is to split the observed transitions into $2I + 1$ transitions.

Electron-Electron Interactions: Exchange and Zero Field Splitting Hamiltonians

When there are more than one unpaired electron in a paramagnetic species, electron-electron interactions can have a significant impact on the energy levels of the system. Exchange and electronic dipolar interactions are the main contributors to the electron-electron terms in the spin Hamiltonian. Exchange energy as described by Dirac is a consequence of the permutation symmetries available to a given set of electrons that must obey the Pauli exclusion principle. The immediate and most common consequence is an energetic separation between states of different multiplicities, *e.g.*, the separation between singlet and triplet states. Electronic dipole-dipole interactions are the magnetic interactions between the electron magnetic moments akin to the hyperfine interaction. These dipolar interactions can lift the degeneracy of the magnetic sublevels at zero applied magnetic field, and this phenomenon is generally referred to as zero-field splitting. Via Kramers theorem, though, in a half integer spin system, each doublet with equal and opposite spin angular momentum will remain degenerate in the absence of a magnetic field (under time reversal symmetry).

For a system of *n* unpaired electrons, we can define a general Hamiltonian that sums over these electron-electron interactions in a pairwise fashion.[18]

$$\widehat{H} = \sum_{\substack{i,j=1 \\ i \neq j, i>j}}^{n} \boldsymbol{S_i} \cdot \boldsymbol{O_{ij}} \cdot \boldsymbol{S_j} \qquad Eq.\,1.17$$

Here, $\boldsymbol{S_i}$ and $\boldsymbol{S_j}$ are the vector operators for electron spin i and j, respectively, and $\boldsymbol{O_{ij}}$ is a rank two tensor describing the interaction between electron i and electron j. In general, a rank two Cartesian tensor is reducible into three irreducible spherical tensors: a scalar isotropic component, an antisymmetric vector product component, and a symmetric and traceless matrix component. The exchange and dipolar Hamiltonians can both be cast into a form as written above with tensors $\boldsymbol{J}$ and $\boldsymbol{D}$.

$$\boldsymbol{J} = \begin{bmatrix} J_{xx} & J_{xy} & J_{xz} \\ J_{yx} & J_{yy} & J_{yz} \\ J_{zx} & J_{zy} & J_{zz} \end{bmatrix}, \boldsymbol{D} = \begin{bmatrix} D_{xx} & D_{xy} & D_{xz} \\ D_{yx} & D_{yy} & D_{yz} \\ D_{zx} & D_{zy} & D_{zz} \end{bmatrix} \qquad Eq.\,1.18$$

It is not always necessary to include all components of the $\boldsymbol{J}$ and $\boldsymbol{D}$ tensors to describe the interactions. For instance, it is often sufficient for molecular systems to include only the isotropic component of exchange, in which case $J_{xy} = J_{xz} = J_{yx} = J_{yz} = J_{zx} = J_{zy} = 0$ and $J_{xx} = J_{yy} = J_{zz} = J$ where J is the isotropic exchange coupling constant. There are also a variety of exchange mechanisms regarding whether the exchange is between two immediate neighboring spin centers (direct exchange), mediated through an intervening atom or set of atoms (superexchange), or whether the spins are delocalized across centers as in conduction electrons (double exchange). Each can contribute to the exchange interaction depending on the nature of the system and can be described in a form as above.[18] The nomenclature here can be confusing, and certain terms are more common in molecular versus solid-state studies. For example, Anderson superexchange

details the isotropic contribution of superexchange, first detailed to explain antiferromagnetism in certain metal oxides. Dzyaloshinskii-Moriya interactions explicitly discuss the antisymmetric component the exchange from superexchange-type mechanisms that arise due to spin-orbit effects, which can be important particularly in magnetic materials.[19–22] Additionally, there are often conflicting conventions even for the form of the isotropic exchange Hamiltonian. The one that we use in this thesis is given below, where a positive J stabilizes the lowest spin multiplicity:

$$\widehat{H}_{ex} = J \sum_{\substack{i,j=1 \\ i \neq j, i>j}}^{n} \sum_{k=x,y,z} \hat{S}_{k_i} \otimes \hat{S}_{k_j} \qquad Eq. 1.19$$

For the zero-field splitting Hamiltonian, the magnetic dipolar interaction between electrons derived via correspondence from the classical dipole-dipole interaction energy gives the form of a symmetric, traceless tensor. Like the g- and A-tensors, it is commonly expressed in its principal axis system:

$$\boldsymbol{D} = \begin{bmatrix} D_x & 0 & 0 \\ 0 & D_y & 0 \\ 0 & 0 & D_z \end{bmatrix} \qquad Eq. 1.20$$

Because of the traceless condition ($D_x + D_y + D_z = 0$), only two values are needed to fully characterize the tensor, and often it is rewritten using the parameters $D = \frac{3}{2} D_z$ and $E = \frac{1}{2}(D_x - D_y)$. D here represents the axial component of the zero-field splitting and can be directly related to geometric considerations such as axial compression or elongation. E represents the transverse components of the zero-field splitting, and although systems that have non-zero E are termed rhombic, there is not always a clear geometric interpretation of this. The signs of D and E are often undetermined, but their absolute value can be experimentally determined. D and E are also

bounded by the condition that $E \leq \frac{1}{3}D$. Spin-orbit coupling also gives rise to a term that is bilinear in electron spins of the form shown here ($\boldsymbol{S} \cdot \boldsymbol{D} \cdot \boldsymbol{S}$). Both dipolar and spin-orbit coupling terms can contribute to the zero-field splitting Hamiltonian. The SOC-derived $\boldsymbol{D}$ tensor need not be traceless, however.[23] In organic systems, it is generally the case that the dipolar interactions are greater than those from SOC, whereas in transition metal systems the reverse is taken to be true. We will write the zero-field splitting Hamiltonian generally as below.

$$\hat{H}_{zfs} = \sum_{\substack{i,j=1 \\ i \neq j, i>j}}^{n} \boldsymbol{S_i} \cdot \boldsymbol{D} \cdot \boldsymbol{S_j} \qquad Eq.\,1.21A$$

When in the principal frame, this Hamiltonian can be written as:

$$\hat{H}_{zfs} = D\left(\hat{S}_z^2 - \frac{1}{3}\hat{S}^2\right) + E\left(\hat{S}_x^2 - \hat{S}_y^2\right) \qquad Eq.\,1.21B$$

Electron Paramagnetic Resonance Spectroscopy

Application of the magnetic field lifts the degeneracy of the $\left|+\frac{1}{2}\right\rangle$ and $\left|-\frac{1}{2}\right\rangle$ states as a function of the magnitude of the external field (Figure 1.7). This generates a spin polarization (and net magnetization) within the sample as the lowest energy eigenstate $\left|-\frac{1}{2}\right\rangle$ will be slightly more populated than the higher energy eigenstate. Electron paramagnetic resonance (EPR) spectroscopy utilizes microwave radiation to probe the transitions between the split spin sublevels. The traditional architecture of an EPR spectrometer involves a microwave source, an amplifier, a magnet, a resonator or cavity into which the sample is placed, and a detector. The resonator is critically coupled to the microwave source, and absorption and emission are detected as a change in the incident microwave intensity that is reflected out of the cavity.[24]

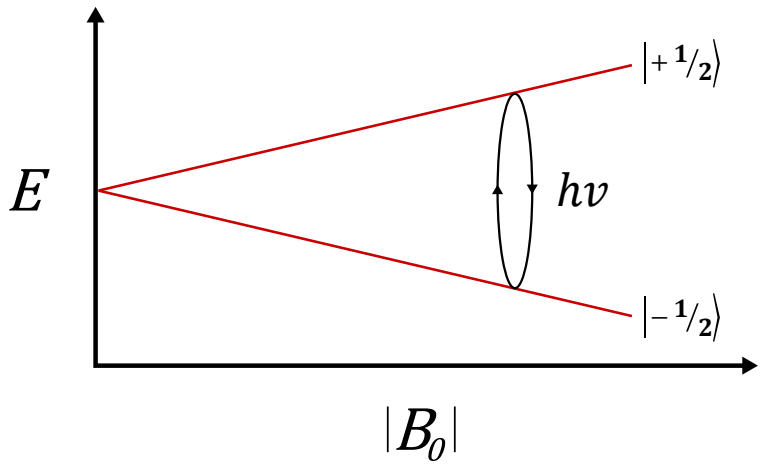

Figure 1.7 Zeeman splitting of the eigenstates of an S = ½ spin system, $\left|+\frac{1}{2}\right\rangle$ and $\left|-\frac{1}{2}\right\rangle$, as a function of the magnitude of the external magnetic field $\boldsymbol{B_0}$. The EPR spectrometer typically uses a tuned microwave frequency that fixes $h\nu$, and thus resonance occurs at specific values of the external magnetic field strength.

Most EPR spectrometers operate at a fixed microwave frequency and instead sweep the permanent magnetic field intensity to generate the absorption spectrum. By changing the magnetic field strength B_0, the splitting between spin sublevels is changed according to the Zeeman component of the spin Hamiltonian. Only when the splitting between particular spin sublevels approaches the microwave energy ($h\nu$) can the resonance condition be fulfilled and absorption/emission occur. There are additional selection rules that govern which transitions couple to the radiation field. The magnetic field component of the microwave radiation, $\boldsymbol{B_1}$, may be polarized perpendicular or parallel to the field lines of the permanent magnet, $\boldsymbol{B_0}$, leading to perpendicular and parallel modes of operation for the spectrometer. When in perpendicular mode, the allowed transitions follow the selection rule $\Delta M_s = \pm 1$. In parallel mode, the allowed

transitions follow $\Delta M_s = \pm 2$. All the EPR spectra presented in this thesis were collected in perpendicular mode.

In continuous wave (CW) EPR, the microwave is continuously applied to the resonator and the magnetic field is swept, generating the absorption spectrum. In practice, the external field is often modulated at a particular frequency and amplitude, lock-in detection is used at the modulation frequency giving higher sensitivity, and the change in microwave intensity as the field is oscillated within the modulation amplitude range is recorded. This means that CW EPR typically provides the first derivative of the absorption spectrum and is how such data is commonly presented.

Pulsed EPR Spectroscopy

Pulsed EPR employs microwave pulses to excite the spin system. Most modern-day nuclear magnetic resonance (NMR) spectrometers also operate in pulsed mode using radiofrequency radiation, and the following is general to all magnetic resonance spectroscopies; however, we choose to contextualize this discussion in terms of EPR. To visualize the action of microwave pulses as well as the various relaxation phenomena, it is helpful to consider the bulk magnetization vector of the sample. In a given EPR sample, there will be many individual spin centers excited by the microwave radiation. At thermal equilibrium, a small but distinguishable greater percentage of electron magnetic moments will be aligned with the externally applied field than anti-aligned as dictated by the Zeeman splitting and corresponding Boltzmann population. This gives rise to a net magnetic moment of the sample aligned with the field (the laboratory +z-axis as we have previously defined). In a classical sense, a magnetic dipole oriented at an angle ($\neq$ 0, 180°) to an external magnetic field will precess about the external field vector at the dipole's Larmor frequency. However, at equilibrium, none of the individual magnetic moments share phase

coherence – they are not precessing in phase with each other. As a result, there is no net x- or y-magnetization and the net magnetization vector $\boldsymbol{M}$ is parallel to the field $\boldsymbol{B_0}$ as depicted in Figure 1.8A.[25,26]

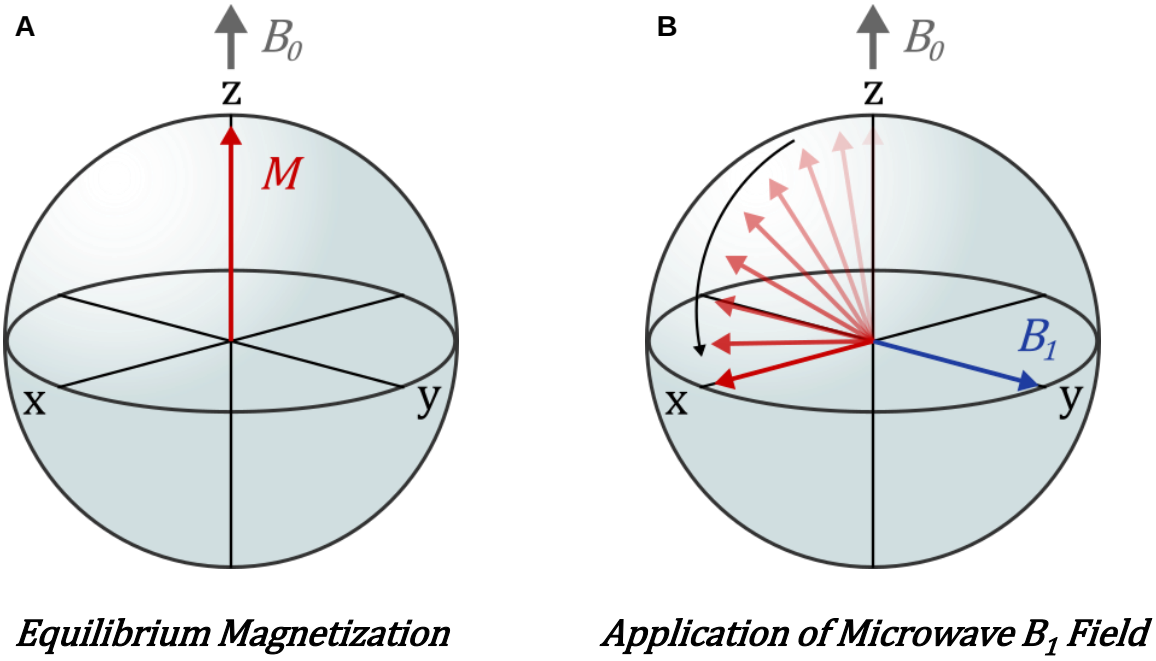

Figure 1.8 (A) The thermal equilibrium picture of the net magnetization vector $\boldsymbol{M}$ of a paramagnetic EPR sample in the externally applied field $\boldsymbol{B_0}$. **(B)** The action of a magnetic field $\boldsymbol{B_1}$ (from the microwave) applied along the +y-axis causes the net magnetization to rotate in the xz plane as portrayed in a rotating reference frame.

A helpful conceit in analyzing the evolution of the magnetization is a rotating reference frame. Once $\boldsymbol{M}$ forms a non-zero angle with $\boldsymbol{B_0}$, $\boldsymbol{M}$ will begin precessing at the Larmor frequency of the system of magnetic moments. If the laboratory reference frame is replaced with a frame that is itself rotating at this Larmor frequency, the complex precessional motion is removed from the

equations of motion. In perpendicular-mode EPR, a linearly polarized microwave is applied such that the magnetic field component of the microwave $\boldsymbol{B_1}$ field is perpendicular to the external field $\boldsymbol{B_0}$ and functions to tip $\boldsymbol{M}$ from its equilibrium position. In our rotating frame, the linearly polarized microwave can be decomposed into a linear combination of left- and right-circularly polarized components. By convention, only the component that rotates with the same sense of the Larmor precession of the spin system is taken as on resonant and the other is discarded. As a result, the $\boldsymbol{B_1}$ field appears static in the rotating frame and can be aligned within the frame by adjusting the phase of the microwave pulse.

We depict the action of $\boldsymbol{B_1}$ aligned along the +y-axis in the rotating frame in Figure 1.8B. Once $\boldsymbol{B_1}$ is turned on, $\boldsymbol{M}$ will begin to rotate in the xz plane about the +y-axis in a process known as Rabi nutation, and the angular frequency with which $\boldsymbol{M}$ precesses about $\boldsymbol{B_1}$ is known as the Rabi nutation frequency (Ω). The Rabi nutation frequency depends on both the magnetic moment being rotated (and therefore the spin angular momentum, characterized by S and M_s, of the excited spin system) as well as the strength of $\boldsymbol{B_1}$.[27]

$$\Omega_{M_s,M_s\pm1} = \omega_1\sqrt{S(S+1) - M_s(M_s \pm 1)} \qquad Eq.\,1.22$$

Here, the microwave field strength is expressed in angular frequency units $\omega_1 = \mu_B g B_1 \hbar^{-1}$. The microwave pulse is applied for a finite time duration τ. As a result, the angle θ that $\boldsymbol{M}$ is rotated by can be predicted using the nutation frequency as $\theta = \Omega\tau$. In fact, most often, pulse sequences are described by the rotation angles that each pulse enacts upon the magnetization. If $\boldsymbol{B_1}$ is applied for a pulse duration such that $\boldsymbol{M}$ is rotated from the +z-axis onto the +x-axis, this is described as a "$\frac{\pi}{2}$ pulse" (Figure 1.8B). As we will see, an important consequence of the spin-

dependent nutation frequency is that pulsed EPR can selectively probe transitions in manifolds of different spin multiplicity in one sample.

An important consideration is that here we have discussed the evolution of the bulk magnetism in terms of purely classical phenomena. However, the bulk magnetization is the macroscopic consequence of the many quantum mechanical spin systems we are probing within the sample. Via correspondence, we can describe the evolution of the classical magnetization *or* the evolution of the quantum mechanical state vector of a two-level system as a function of the applied fields. The state vector can similarly be represented in an axis system like what we have drawn for the magnetization in Figure 1.8, and this representation is known as the Bloch sphere. Rather than changing the amplitudes of x-, y-, and z-components of magnetization, the state vector evolves through changing complex probability amplitudes in the wavefunction brought on by the $\boldsymbol{B_1}$ field.

Paramagnetic Relaxation

Let us say we have performed a $\frac{\pi}{2}$ pulse as depicted in Figure 1.8B. The net magnetization is now perpendicular to the z-axis: the z-component of $\boldsymbol{M}$ is zero, and the phase coherence given to the spins via the microwave pulse has generated maximum transverse magnetization aligned along the x-axis. After the pulse is applied, this is a nonequilibrium state of the system. Over time, relaxation will return the magnetization back to its thermal equilibrium alignment along the z-axis. This complex relaxation can be decomposed into two separate processes. The first is relaxation of the z-component of magnetization back to its full equilibrium value (described as longitudinal relaxation and denoted by T_1). The second is the loss of phase coherence of the excited spin packet

and return of the x- and y-components of magnetization back to zero (described as transverse relaxation and denoted by T_2). These relaxation processes are depicted in Figure 1.9A and B.[14,25,28]

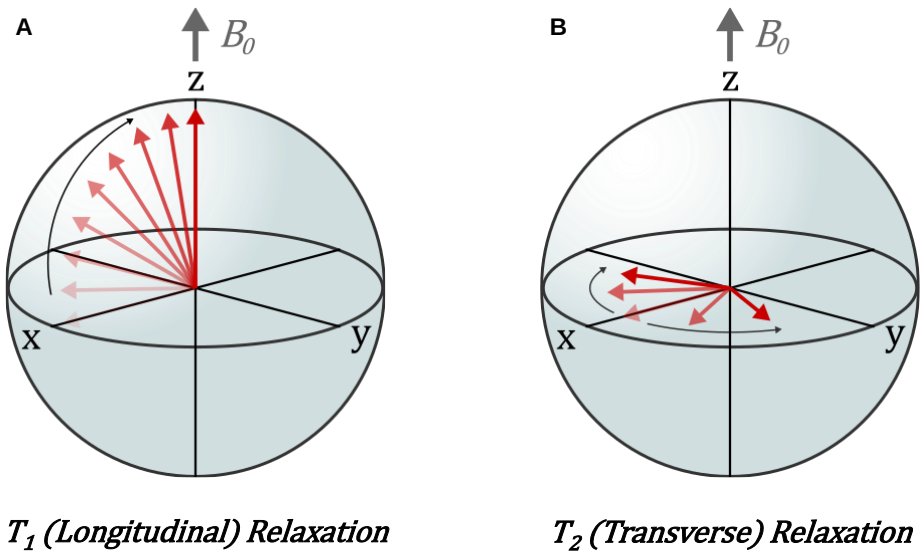

Figure 1.9 (A) Visualization of T_1, longitudinal relaxation or the return of the z-component of the magnetization. **(B)** Visualization of T_2, the transverse relaxation or loss of phase coherence / the x- and y-components of magnetization.

T_1 is sometimes referred to as spin-lattice relaxation. As this name suggests, T_1 relaxation arises due to an exchange of energy between the spin system and the surrounding environment. In solution-state NMR, it is generally the molecular tumbling motion that gives rise to the appropriate spectral density that can exchange energy with the nuclear spin system. In solid-state EPR, however, the molecular motions responsible for T_1 relaxation are generally lattice phonons and low-energy librations.

T_2, on the other hand, is sometimes referred to as spin-spin relaxation. Spin "flip-flop" processes in which two spins exchange their spin angular momentum does not affect the

longitudinal magnetization but can lead to dephasing of the transverse magnetization. Other phenomena can contribute to T_2 beyond spin-spin interactions, however. Dynamic fluctuations in local magnetic field, which can be due to other sources of magnetic fields in the sample such as nuclei, can give rise to instantaneous jumps in Larmor frequencies of particular spin packets, which leads to the loss of phase coherence as well.

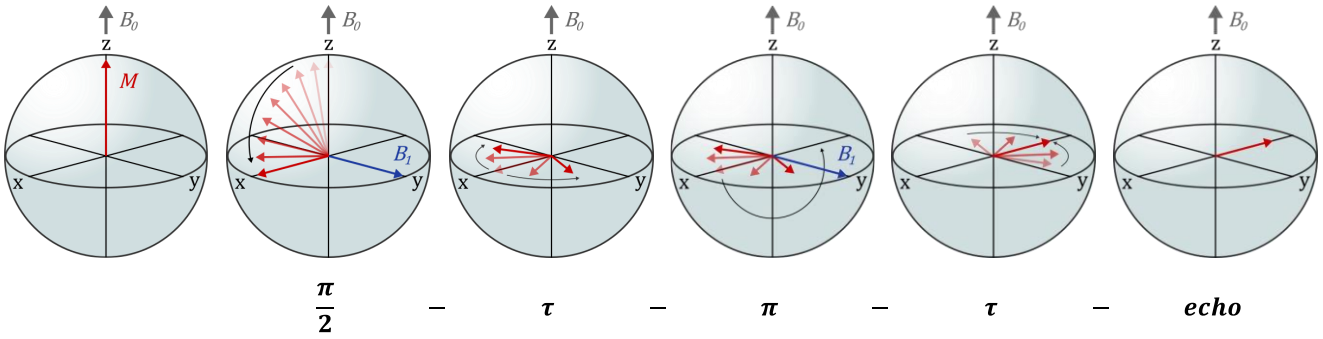

Figure 1.10 A visualization of the Hahn echo pulse sequence: $\frac{\pi}{2} - \tau - \pi - \tau - echo$. Static inhomogeneities that give rise to slightly different Larmor frequencies of the spin packets are refocused into an observable echo signal.

Transverse relaxation is commonly measured using a Hahn echo pulse sequence with varying delay times.[29] The Hahn echo sequence is defined in terms of the turning angles of the pulses as follows: $\frac{\pi}{2} - \tau - \pi - \tau - echo$ as shown in Figure 1.10. The $\frac{\pi}{2}$ pulse tips the magnetization into the transverse plane. The system is allowed to evolve for time τ, during which the spins will begin to dephase. A portion of the transverse magnetization loss will be due to spin relaxation, and a portion will be due to static inhomogeneities that cause various spins to precess and slightly different Larmor frequencies from each other. A π pulse rotates the magnetization by 180 ° while preserving the sense of rotation of the various spins, which results in a refocusing of

the spins after an additional time τ. A photon echo is then detected at a time 2τ after the initial $\frac{\pi}{2}$ pulse. The intensity of the photon echo will be proportional to how many of the spins may be refocused by the π pulse. The π pulse can refocus the magnetization loss caused by the static inhomogeneities (reversible), but not that caused by spin relaxation (irreversible). By observing the loss of echo intensity as a function of increasing the delay time t, the transverse relaxation rate can be estimated.

The echo intensity observed in the Hahn echo sequence can also be impacted by spectral diffusion. The bandwidth of microwave excitation is often much less than the linewidth of a given EPR spectrum. As a result, the excitation energy imparted to one spin packet may be exchanged with other off-resonant spins due to overlaps in the spin packet bandwidths. If a portion of the excitation population is moved out of resonance with the microwave radiation, it cannot be refocused by the π pulse. This contributes to the loss of echo intensity but is not directly T_2 relaxation. Because of this, often the experimentally derived relaxation time from a Hahn echo sequence is termed T_M, the phase memory time, which includes the contributions of T_2 as well as these diffusive processes.

T_1 can be estimated using an inversion recovery pulse sequence. Here, an initial π pulse is used to invert the magnetization to lie along the –z-axis. The spins are allowed to relax over time τ, during which the spins will reapproach their equilibrium alignment with the external field. The longitudinal magnetization is read out using a Hahn echo pulse sequence with a fixed delay time t. The T_1 relaxation time is then determined by varying the waiting time τ after the initial π pulse. As the magnetization is initially inverted, the phase of the echo will also be offset by 180 °, which is usually taken to be a negative signal relative to the positive signals detected in the standard Hahn echo sequence. As the magnetization relaxes back to its alignment along the +z-axis, the observed

echo intensity follows the magnetization beginning negative, passing through zero, and finally becoming positive until the equilibrium magnetization is recovered.

Theoretically, T_1 and T_2 are considered to follow first-order kinetics and exhibit monoexponential decay functions. In practice, however, diffusion processes and the distribution of spin packets excited by the microwave pulse often lead to stretched exponential behavior.

In summary, in this section we have examined spin angular momentum and the magnetic interactions in a system of unpaired electrons, constructing a spin Hamiltonian that can be used to calculate the small energetic splittings. EPR interrogates these level splittings and gives us information on the electronic structure of the system in the form of fitted parameters (e.g. the $\boldsymbol{g}$, $\boldsymbol{A}$, $\boldsymbol{J}$, and $\boldsymbol{D}$ tensors). Pulsed-EPR can provide information with respect to the longitudinal (T_1) and transverse magnetic (T_2) relaxation properties of the system.

Citations

(1) Siebrand, W. Nonradiative Processes in Molecular Systems. In *Dynamics of Molecular Collisions: Part A*; Miller, W. H., Ed.; Springer US: Boston, MA, 1976; pp 249–302. https://doi.org/10.1007/978-1-4615-8867-2_6.

(2) Bixon, M.; Jortner, J. Intramolecular Radiationless Transitions. *J. Chem. Phys.* **1968**, *48* (2), 715–726. https://doi.org/10.1063/1.1668703.

(3) Robinson, G. W.; Frosch, R. P. Electronic Excitation Transfer and Relaxation. *J. Chem. Phys.* **1963**, *38* (5), 1187–1203. https://doi.org/10.1063/1.1733823.

(4) Jortner, J.; Bixon, M. Radiationless Transitions in Polyatomic Molecules. *Israel Journal of Chemistry* **1969**, *7* (2), 189–220. https://doi.org/10.1002/ijch.196900032.

(5) Englman, R.; Jortner, J. The Energy Gap Law for Radiationless Transitions in Large Molecules. *Molecular Physics* **1970**, *18* (2), 145–164. https://doi.org/10.1080/00268977000100171.

(6) Berera, R.; van Grondelle, R.; Kennis, J. T. M. Ultrafast Transient Absorption Spectroscopy: Principles and Application to Photosynthetic Systems. *Photosynth Res* **2009**, *101* (2), 105–118. https://doi.org/10.1007/s11120-009-9454-y.

(7) Mukamel, S. *Principles of Nonlinear Optical Spectroscopy*; Oxford University Press, 1995.

(8) Lorenc, M.; Ziolek, M.; Naskrecki, R.; Karolczak, J.; Kubicki, J.; Maciejewski, A. Artifacts in Femtosecond Transient Absorption Spectroscopy. *Appl Phys B* **2002**, *74* (1), 19–27. https://doi.org/10.1007/s003400100750.

(9) van Stokkum, I. H. M.; Larsen, D. S.; van Grondelle, R. Global and Target Analysis of Time-Resolved Spectra. *Biochimica et Biophysica Acta (BBA) - Bioenergetics* **2004**, *1657* (2), 82–104. https://doi.org/10.1016/j.bbabio.2004.04.011.
(10) Mullen, K. M.; Stokkum, I. H. M. van. TIMP: An R Package for Modeling Multi-Way Spectroscopic Measurements. *Journal of Statistical Software* **2007**, *18*, 1–46. https://doi.org/10.18637/jss.v018.i03.
(11) Snellenburg, J. J.; Laptenok, S.; Seger, R.; Mullen, K. M.; Stokkum, I. H. M. van. Glotaran: A Java-Based Graphical User Interface for the R Package TIMP. *Journal of Statistical Software* **2012**, *49*, 1–22. https://doi.org/10.18637/jss.v049.i03.
(12) McWeeny, R. *Spins in Chemistry*; Dover Publications, 2004.
(13) McWeeny, R. On the Origin of Spin-Hamiltonian Parameters. *J. Chem. Phys.* **1965**, *42* (5), 1717–1725. https://doi.org/10.1063/1.1696183.
(14) Weil, J. A.; Bolton, J. R. Basic Principles of Paramagnetic Resonance. In *Electron Paramagnetic Resonance*; John Wiley & Sons, Ltd, 2006; pp 1–35. https://doi.org/10.1002/9780470084984.ch1.
(15) Abragam, A. *Electron Paramagnetic Resonance of Transition Ions*; Oxford Classic Texts in the Physical Sciences; Oxford University Press: Oxford, New York, 2012.
(16) Abragam, A. *The Principles of Nuclear Magnetism.*; Clarendon Press: Oxford, 1961.
(17) Solomon, E. I. Introduction. *Comments on Inorganic Chemistry* **1984**, *3* (5), 227–229. https://doi.org/10.1080/02603598408080072.
(18) Bencini, A.; Gatteschi, D. *EPR of Exchange Coupled Systems*; Courier Corporation, 2012.
(19) Anderson, P. W. Antiferromagnetism. Theory of Superexchange Interaction. *Phys. Rev.* **1950**, *79* (2), 350–356. https://doi.org/10.1103/PhysRev.79.350.
(20) Anderson, P. W. New Approach to the Theory of Superexchange Interactions. *Phys. Rev.* **1959**, *115* (1), 2–13. https://doi.org/10.1103/PhysRev.115.2.
(21) Dzyaloshinsky, I. A Thermodynamic Theory of "Weak" Ferromagnetism of Antiferromagnetics. *Journal of Physics and Chemistry of Solids* **1958**, *4* (4), 241–255. https://doi.org/10.1016/0022-3697(58)90076-3.
(22) Moriya, T. Anisotropic Superexchange Interaction and Weak Ferromagnetism. *Phys. Rev.* **1960**, *120* (1), 91–98. https://doi.org/10.1103/PhysRev.120.91.
(23) Boča, R. Zero-Field Splitting in Metal Complexes. *Coordination Chemistry Reviews* **2004**, *248* (9), 757–815. https://doi.org/10.1016/j.ccr.2004.03.001.
(24) Chechik, V.; Carter, E.; Murphy, D. *Electron Paramagnetic Resonance*; Oxford University Press, 2016.
(25) Schweiger, A.; Jeschke, G. *Principles of Pulse Electron Paramagnetic Resonance*; Oxford University Press, 2001.
(26) Hore, P. J.; Jones, J. A.; Wimperis, S. *NMR: The Toolkit : How Pulse Sequences Work*; Oxford University Press, 2015.
(27) Stoll, S.; Jeschke, G.; Willer, M.; Schweiger, A. Nutation-Frequency Correlated EPR Spectroscopy: The PEANUT Experiment. *Journal of Magnetic Resonance* **1998**, *130* (1), 86–96. https://doi.org/10.1006/jmre.1997.1285.
(28) Eaton, S. S.; Eaton, G. R. Relaxation Times of Organic Radicals and Transition Metal Ions. In *Distance Measurements in Biological Systems by EPR*; Berliner, L. J., Eaton, G. R., Eaton, S. S., Eds.; Springer US: Boston, MA, 2000; pp 29–154. https://doi.org/10.1007/0-306-47109-4_2.

(29) Hahn, E. L. Spin Echoes. *Phys. Rev.* **1950**, *80* (4), 580–594. https://doi.org/10.1103/PhysRev.80.580.